

# A Fast 3-D Approach for Electroporation Treatment Planning: Optimal Electrodes Configuration

A. Paffi , F. Apollonio , *Senior Member, IEEE*, M. Cadossi, V. D'Alessio, R. Fusco, A. Giannini, and M. Liberti , *Senior Member, IEEE*

**Abstract**—Purpose of this work is to develop a tool for electrochemotherapy treatment planning, which automatically estimates the optimal electrode configuration on the basis of the calculation of the induced electric field in a 3D tissue volume, including the tumor lesion, obtained from patient's MRI. The tool conciliates accuracy in the estimate of the tumor coverage with speed of calculation. The optimal electrodes configuration, that guarantees the tumor electroporation with the minimum number of electrodes, is obtained by adapting algorithms for the creation of unstructured simplex meshes. To go fast, the elementary electric field distributions are pre-calculated and stored in a database and the optimization procedure is split in two consequential steps: transversal and longitudinal optimizations. The whole code is implemented in C++ environment. The tool, tested in a set of real cases, showed the complete electroporation of the lesions, while preserving noble structures from the electrodes crossing. Calculation times were compatible with real-time requirements. The proposed tool represents a valid support for the electroporation treatment planning. With respect to the literature, it automatically estimates the best electrode configuration in a realistic 3D domain, while maintaining reduced calculation times. This is crucial for improving effectiveness and reliability of electroporation-based treatments.

**Index Terms**—Computational electromagnetics, dosimetry, medical treatment, optimization methods, planning.

## I. INTRODUCTION

**E**LECTROCHEMOTHERAPY (ECT) is a well-known, non-thermal methodology that can be defined as locally enhanced chemotherapy because combines the administration of chemotherapeutic drugs with well-defined electric (E) field pulses that induce the reversible cell membrane electroporation (EP) [1], [2]. ECT is indicated for the treatment of patients with unresectable tumors, resulting in amelioration of quality of life and is often offered to patients previously treated with radiotherapy or in patients undergoing chemotherapy, to control the local disease [3], [4], [5]. Preliminary data on ECT in association with immunotherapy are also available [6].

Since the adoption of the European Standard Operating Procedure (ESOP) protocol [7], [8], its safety and effectiveness

has been proved in many solid tumors clinical trials. Most of the observed adverse events are local and transient and no serious adverse events or deaths have been reported [9]. The effectiveness of ECT with bleomycin has been observed in several cutaneous and subcutaneous tumors [1], [2], [10], [11], [12], [13], [14], [15], [16], [17], [18] and, more recently, its use was extended to treat solid tumors of liver and pancreas, in both preclinical and clinical studies [19], [20], [21], [22], [23], [24], [25]. ECT, being a non-thermal technique, has the advantage that the treatment of lesions located near noble structures, such as vessels and bile ducts, is possible without damage.

Although ECT can be used for the treatment of various malignant lesions, some limitations still occur. In particular, in the case of big lesions, correct positioning of the electrodes, usually individual long needles, is mandatory to ensure the effective EP of the whole tumor lesion (TL) [26], [27], [28].

Technical developments have improved ECT equipment, with custom electrode probes and dedicated tools supporting individual treatment planning in anatomically challenging tumors.

The correct spatial configuration of the needle electrodes requires skill and the support of intraoperative imaging: x-ray, ultrasound, or computed tomography imaging [29]. Specific instruments have been developed to guide needle insertion and positioning and to guarantee the complete and homogenous EP of the TL [27]. The drawback of incorrect electrode positioning may be insufficient EP in the target tissue, thus increasing the risk of partial responses and local recurrences [29], [30].

Treatment needs to be carefully planned with dedicated software that indicates where to place electrodes and the required EP pulse conditions [31], [34].

Some tools have been recently developed to facilitate the treatment planning by calculating and visualizing the induced E field [31], [32], [33], [34], [35], [36], [https://view.upf.edu/], but only one of them couples this kind of calculation with the automatic estimate of the best electrode configuration (PULSAR, IGEA S.p.A.) in a 2D domain [37].

In this paper, we propose a new tool for patient-specific ECT treatment planning which automatically estimates the best electrodes configuration in a 3D domain while maintaining short calculation times typical of the 2D approach [37]. The software core is the automatic calculation of the optimal needles configuration, integrated with the 3D estimate of the E-field distribution inside the whole domain. It should be noticed that the optimal configuration is not unique but is one of the possible configurations that guarantees the complete EP of the region of

Manuscript received 22 November 2023; revised 15 April 2024; accepted 19 May 2024. (Corresponding author: A. Paffi.)

A. Paffi, F. Apollonio, and M. Liberti are with the Department of Information Engineering, Electronics and Telecommunications (DIET), Sapienza University of Rome, 00185 Rome, Italy (e-mail: alessandra.paffi@uniroma1.it).

M. Cadossi, V. D'Alessio, R. Fusco, and A. Giannini are with the IGEA S.p.A., 41012 Carpi, MO, Italy.

Digital Object Identifier 10.1109/JERM.2024.3409678

interest (ROI) using the minimum number of electrodes and preserving noble structures. To identify the optimal needles placement, algorithms of mesh generation, typically used in computer graphics, have been here adapted, for the first time, to this kind of application.

## II. METHODS AND PROCEDURES

### A. Requirements

The first requirement for ECT is the induced E field in the ROI to overcome the threshold for the reversible EP. Using the ESOPE protocol (8 rectangular pulses, 100 kV/m, 100  $\mu$ s), this threshold was estimated to be 40 kV/m [7], [8].

For treatments using needle electrodes to reach deep regions, another important requirement is to minimize the invasiveness by reducing the number of electrodes, while maintaining the coverage of the ROI. The ROI usually coincides with the TL surrounded by a margin chosen by the surgeon.

To avoid damage to noble anatomical structures, such as important blood vessels or nerves, the surgeon can define regions forbidden to the passage of the electrodes, referred to as forbidden regions (FRs).

Besides fulfilling such requirements, the code should also foresee the possibility for the surgeon of manually choosing the position of some of the electrodes, referred to as “fixed electrodes”. The fixed electrode position can be used as a surgical reference to guide the other needles insertion.

The analysis domain here considered is a homogeneous cube, 10 cm of side, including the 3D reconstruction, based on segmentation of the patient DICOM images, of the ROI and the FRs.

The needle electrodes are inserted almost parallel to each other with an insertion angle selected by the surgeon to facilitate the access to the ROI and to preserve FRs. Therefore, the cubic 3D analysis domain is rotated in order to have the upper face orthogonal to the needles direction which coincides with the  $z$ -axis of our reference system.

According to the ESOPE standard protocol [7], [8], the electrodes are activated in pairs with an applied voltage difference of 1000 V multiplied by their distance, in centimeters. After the activation of all possible couples of electrodes, all points in the ROI must have experienced an E field higher than 40 kV/m at least once. The minimum and the maximum distances between two electrodes of a couple are limited by the dynamics of the generator and the electrode type. As example, using Cliniporator with the sterile disposable needles VGD series (diameter 1.8 mm) from IGEA Clinical Biophysics, these minimum and maximum distances are 0.5 and 3 cm, respectively.

To be suitable for the treatment planning, the automatic calculation of the optimal electrodes configuration should be performed in real-time, i.e., it should take at most some minutes.

The software output is a file containing the coordinates of the needles tips with respect to a defined reference system, the list of the activated electrode couples, with their distances, and the E-field distribution in the 3D domain.

TABLE I  
LIST OF SOFTWARE REQUIREMENTS

<i>Kind</i>	<i>Description</i>
<i>Electromagnetic</i>	1 Calculation of the E-field distribution in the whole 3D domain
	2 E field higher than 40 kV/m in the ROI <sup>a</sup>
<i>Geometric</i>	3 Use the minimum number of electrodes which fulfill req. 2
	4 Distance between activated couples $\in [0.5-3]$ cm <sup>b</sup>
	5 Possibility of placing one or more needles in fixed positions
	6 Preserve FRs
<i>Input/Output</i>	7 Input files: electrodes size; positions of possible fixed electrodes; ROI and FR geometries
	8 Output files: electrodes positions; list of the activated couples and distances; E-field distribution
<i>Computation time</i>	9 Some minutes at most

<sup>a</sup>According to the ESOPE Standard Protocol; <sup>b</sup>with the sterile disposable needles VGD series (diameter 1.8 mm) from IGEA Clinical Biophysics.

Table I summarizes all the software requirements classified in electromagnetic, geometric, on the input/output and on the computation time.

### B. Algorithm Architecture

The core of the treatment planning code is the algorithm that automatically calculates the best position of the electrodes and the couples to be sequentially activated to electroporate the whole ROI. Figure 1 shows a block diagram of the algorithm architecture.

The algorithm, implemented in C++ environment, takes as input the 3D representation of the ROI and the FRs, the electrode typology (i.e., diameter and length of the active contacts), the positions of the possible fixed electrodes and provides as output: i) the electrodes positions, in terms of the Cartesian coordinates of the tips with respect to the defined reference system; ii) the list of the activated electrodes pairs with their distances; iii) the calculated distribution of the induced E field in the whole 3D domain.

To fulfill the constraint of the computation time, two main strategies have been implemented: the decoupled calculation of transversal and longitudinal best electrode positioning and the buildup of a database containing pre-calculated E-field distributions induced by all the possible electrode couples.

Because of the needles are inserted almost parallel to each other, their distances remains the same for any depth from the body surface. Therefore, the procedure for the automatic calculation of the optimal needles configuration can be divided into: a transversal optimization, where the transversal coordinates ( $x$  and  $y$  in our reference system) of the needles are calculated, and a longitudinal optimization, where the  $z$  coordinate of the needle’s tip is given (see Fig. 1). The possibility of calculating separately, in two subsequent steps, transversal and longitudinal optimizations allows us to reduce the degrees of freedom and complexity of the problem, thus reducing computation time.

Once the transversal configuration is calculated, the resulting electroporated region along the  $z$  axis could be smaller than the

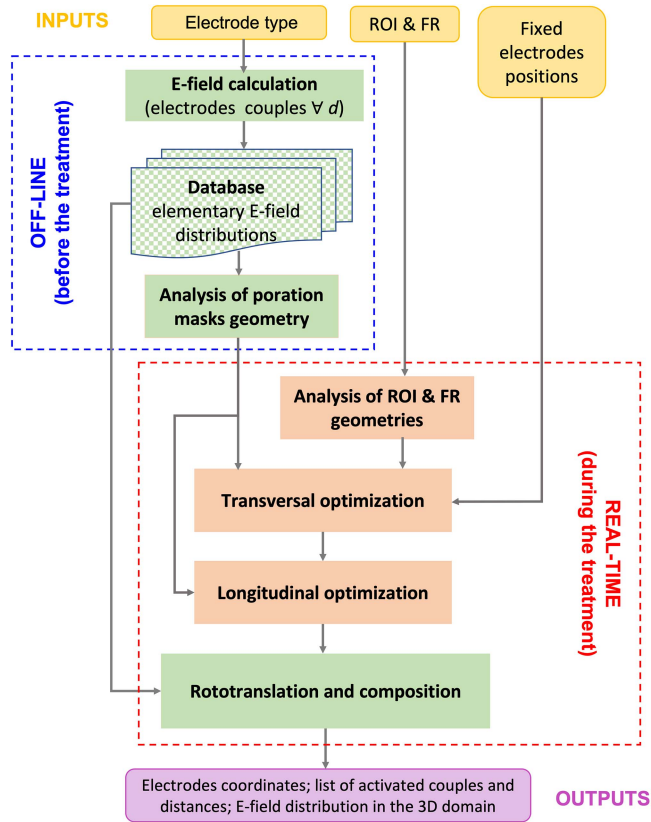


Fig. 1. Block diagram describing the implementation strategy and the operation flow.

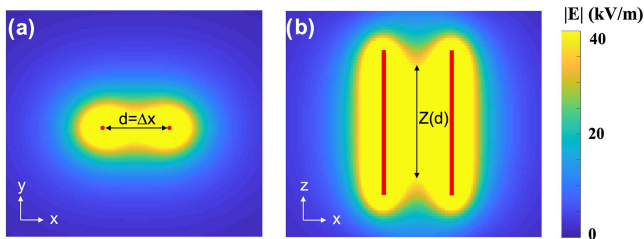


Fig. 2. Example of elementary E-field distribution on the  $xy$  and  $xz$  planes for electrodes (in red) 1.2 mm of diameter, 30 mm of length, 20 mm of distance ( $d$ ). The light yellow geometry identifies the “poration mask” where  $|E|$  overcomes 40 kV/m;  $Z$  is the  $z$ -size of the poration mask.

ROI  $z$ -size. Therefore, it could be necessary to repeat the treatment delivery after shifting one or more times the needles’ tips along  $z$ . Such shifts will be referred to as “deployments”. In the longitudinal optimization, the number of different deployments and the related  $z$  coordinates of the needle tips are returned.

Another strategy to reduce the computation time derives from the consideration that, in any configuration, the electrodes are always activated in couple with the applied voltage difference defined by the electrode distance [7], [11].

Therefore, for each kind of electrodes, it is possible to calculate off-line, before the treatment, once and for all, the E-field distributions generated in the 3D analysis domain by a couple of electrodes placed centrally, as in Fig. 2, at a set of distances  $d = \Delta x$  from  $d_{\min} = 0.5$  cm to  $d_{\max} = 3$  cm with step  $\Delta d = 1$  mm.

These results are stored in a database of 26 files, for each kind of electrodes, containing the “elementary E-field distributions” (Fig. 2).

### C. Procedure for the E-field Calculation

To calculate these distributions, we used the admittance method [38], [39] where the magnetic sources were disregarded and the voltage difference between the electrodes was applied as a boundary condition. The analysis domain was divided into  $N$  cubic cells of homogeneous material ( $\sigma = 0.4$  S/m;  $\epsilon_r = 78$ ) [30], with  $N$  depending on the desired spatial resolution. The cells occupied by the electrodes were assigned to steel ( $\sigma = 1.45 \times 10^6$  S/m). The current conservation condition was applied to the outer boundary.

The volume where the E-field distribution overcomes the EP threshold is referred to as “poration mask” and is mathematically defined as:

$$\text{poration mask} = \cup_{i,j,k} v(i, j, k); \text{ if } |E(i, j, k)| \geq 40 \frac{kV}{m}, \quad (1)$$

where  $\cup$  is the union operator,  $v(i, j, k)$  is the voxel in the  $(i, j, k)$  position.

As evident from Fig. 2, the poration mask on the  $xy$  and  $xz$  planes, for a couple of electrodes, has a shape with a narrowing between the two electrodes. In the  $xz$  plane, the minimum height  $Z(d)$  depends on the electrodes distance  $d$  and could be shorter than the length of the active contacts.

Information on the poration masks geometry is used for the transversal and longitudinal optimization.

The final induced E-field distribution is calculated as follows: for each couple of activated electrodes, the corresponding “elementary E-field distribution” is loaded from the database; it is shifted and oriented (rototranslation) so that the positions of the electrodes in the reference system used to calculate the elementary E-field distribution coincide with the actual electrodes coordinates, except for the discretization error; for each voxel, the maximum E-field value experienced is retained (composition). The time spent in this procedure is compatible with real time requirements and is essentially dominated by the loading time of the matrices from the database.

### D. Procedure for Optimization of the Needle Configuration

The input information provides size and geometry of the ROI and the possible FRs. As an example, Fig. 3(a) shows three transversal slices of a ROI (red) and FR (blue), coming from MRI of a liver metastasis, at the  $z$ -quotes: 20, 40 and 60 mm. To guarantee that the estimated electrode configuration electroporates all the ROI transversal sections, it must electroporate the projection of the ROI on a generic transversal plane, orthogonal to the electrodes, referred to in the following as  $xy$  plane (Fig. 3(b)). Since the ROI projection may assume very irregular geometries, to simplify the problem, we start considering the poration of the circumscribed rectangle  $S_0$  (Fig. 3(b)).

The procedure for the transversal optimization is summarized in the flow-chart of Fig. 4.

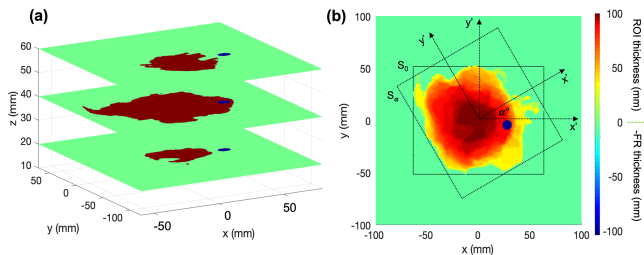


Fig. 3. (a) ROI (red) and FR (blue) transversal sections; (b) projection of the ROI and the FR on the  $xy$  plane. The color is associated to the thickness of the ROI (positive values) or minus the thickness of the FR (negative values).  $S_0$  is the rectangle circumscribed to the ROI projection;  $S_\alpha$  is the circumscribed rectangle in the  $x'y'$  system rotated of  $\alpha^\circ$  around the  $z$  axis through the centroid.

After extracting the projections on the  $xy$  plane of the ROI and FRs, a new reference system  $x'y'$  is considered with the origin coincident with the centroid of the ROI projection (Fig. 3(b)). This system is rotated around the vertical  $z$  axis through the centroid of  $\alpha^\circ$  between  $0^\circ$  and  $180^\circ$  with step  $3.75^\circ$ . For each of the 48 rotations, the circumscribed rectangle  $S_\alpha$  is calculated (Fig. 3(b)) and that with the smallest area ( $S_\alpha = S^*$ ) is selected (step 1 in Fig. 4). This allows us to minimize the area of healthy tissue included in  $S^*$  and thus affected by EP. After that, the procedure follows two different paths depending on whether  $S^*$  can be completely electroporated with standard electrode configurations or not.

In ECT, standard electrode configurations are often used to treat small ROIs: i) a couple of electrodes with distance  $d$  between 0.5 and 3 cm; ii) three electrodes placed in the vertexes of an equilateral triangle with sides between 0.5 and 3 cm; iii) four electrodes placed in the vertexes of a rectangle with sides longer than 0.5 cm and diagonal shorter than 3 cm; iv) five electrodes placed in the vertexes and in the center of a rectangle with sides between 0.5 and 3 cm. In configuration iii, 6 combinations of poles are activated in sequence: the four sides and the two diagonals; in configuration iv, 8 combinations are activated: the couples on the four sides and those between each vertex and the center.

The simplest configuration (smallest and with the minimum number of electrodes) providing the full coverage of  $S^*$  with a suprathreshold E field is chosen as the optimal one.

If any electrodes (nodes) are inside the FR, they are moved outside (step 6 of Fig. 4) in a way that all the activated couples are preserved (distances between 0.5 and 3 cm).

Finally, in step 7, possible fixed electrodes are added; if one of the calculated nodes is too close to the fixed ones, it is removed.

If standard configurations are not suitable to cover the ROI, a different approach is followed. From the standard configurations, we know that when the electrodes are placed in the vertexes of a triangle with sides shorter than a well-defined length (i.e., 3 cm), the whole area inside the triangle is electroporated, plus a margin surrounding the triangle perimeter. So, a triangle can be used as a basic shape to build up a mesh. The ROI projection defines a planar geometry that must be approximated with a triangular mesh, analogously to what occurs in computer graphics [40] and in scientific computing using Finite Element Method

(FEM) [41]. Differently from other applications, where the goal is to minimize the error in approximating curved boundaries, even if this may require a huge number of elements, here we want to use the minimum number of triangles, with the constraint that the length of the triangle sides is between 0.5 and 3 cm. The triangles vertexes are the mesh nodes and define the electrodes positions; the triangles sides define the couples of poles that can be activated and their lengths are the distances between poles.

To generate the unstructured simplex mesh, we started from the algorithm described in [42], based on the physical analogy between a simplex mesh and a truss structure. The final node locations are found by solving for equilibrium in a truss structure subjected to external forces [42].

The procedure, adapted to our case, is described in steps 3, 4, and 5 of Fig. 4.

After defining the smallest  $S^*$  containing the ROI, a regular mesh (3 cm of side) of equally spaced nodes is created and a Delaunay triangulation [43] is applied to fully cover  $S^*$  with a surface of  $N$  triangles (step 3 in Fig. 4).

In step 4, all the triangles whose centroid lies outside the ROI are deleted (Fig. 4). This procedure may leave uncovered some portions of the ROI, whereas some external electrodes may be quite far from the ROI boundary and from the other electrodes, requiring an unnecessary high voltage difference to be applied. Therefore, all the nodes lying close to the ROI boundary (between the two magenta curves in step 5 of Fig. 4) are subjected to attractive forces orthogonal to the ROI boundary and proportional to the distance from it (purple arrows in step 5 of Fig. 4 represent these external forces). Contemporarily, the triangles sides (bars) react, like ordinary linear springs, exerting on the nodes forces proportional to  $l-l_0$ , where  $l$  is the current bar length and  $l_0$  the desired mesh size.

The forces  $\mathbf{F}$  move the nodes  $\mathbf{p}$  until a static force equilibrium in the structure is reached:

$$\mathbf{F}(\mathbf{p}) = 0, \quad (2)$$

To find the final nodes configuration, we consider the system of ODEs:

$$\frac{d\mathbf{p}}{dt} = \mathbf{F}(\mathbf{p}) \quad t \geq 0, \quad (3)$$

which is solved using the forward Euler method. For each  $\mathbf{p}$  update, the Delaunay triangulation is performed iteratively and the array of forces is recalculated. The escape from the iteration occurs if either the nodes shift is below a fixed tolerance level or the triangle side is longer than  $l_0 = 30$  mm. Further details on the algorithm implementation can be found in [42].

The transversal configuration determines a 3D E-field distribution and a related poration mask. A critical parameter is the minimum size of the poration mask along  $z$  ( $Z_{TOT}$ ), which depends on the distance  $d$  between the electrodes of the activated couples. As a rough conservative rule,  $Z_{TOT}$  is considered equal to  $Z(d_{max})$  (see Fig. 2(b)), i.e., the  $z$ -size of the elementary poration mask corresponding to the activated couple with the maximum distance.

If  $Z(d_{max})$  is larger than the maximum  $z$ -size of the ROI, the longitudinal optimization only returns the  $z$ -coordinate of the

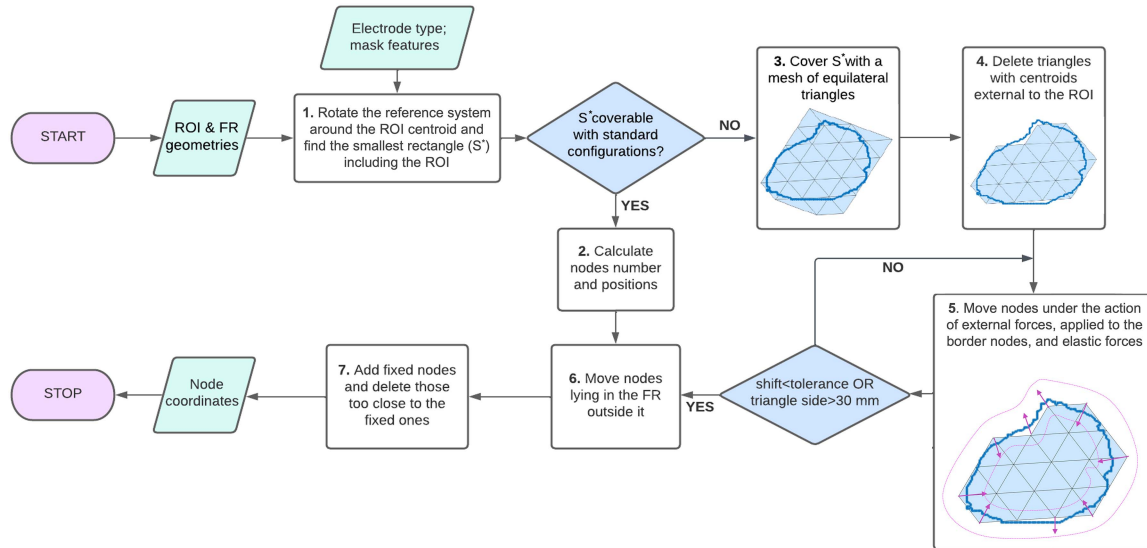


Fig. 4. Flow chart of the procedure for the calculation of the electrode configuration on the transversal plane.

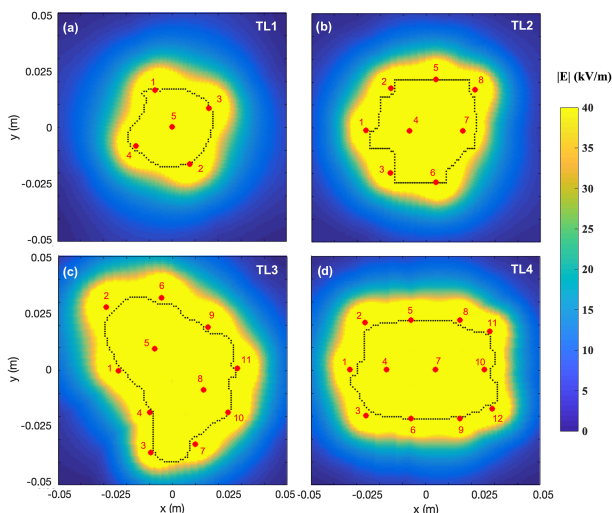


Fig. 5. Examples of electrode configurations (red dots) and induced E field in the transversal  $xy$  plane for TL1 (panel a), TL2 (panel b), TL3 (panel c), and TL4 (panel d); dotted black lines delimit the TL projections on the  $xy$  plane.

electrodes tip to include the ROI in the poration mask, otherwise the number and size of deployments needed to treat the whole ROI along the  $z$ -axis are also calculated.

### III. RESULTS

#### A. Examples of Application

The whole code was tested in a significant set of real TLs, with different shape and size, as study cases of treatment planning.

Fig. 5 shows four examples of electrode configuration and induced E-field distribution on a transversal plane ( $xy$ ) for TLs of interest, ranging from about 3 to 7 cm, obtained from patients' MRI. The dotted black curves in Fig. 5 delimit the projections of the TLs on the  $xy$  plane, the red dots identify the needle positions and the E-field is represented with the full-scale equal

to the poration threshold (40 kV/m), so that the yellow surface represents the electroporated region. The spatial resolution used for the E-field calculation is 0.6 mm. In the example of Fig. 5(a) (TL1), a standard 5-electrode (8 activated couples) configuration is sufficient to ensure full coverage of the TL, whereas, 8 (14 activated couples), 11 (21 activated couples), and 12 electrodes (23 activated couples) are needed to treat TL2 (Fig. 5(b)), TL3 (Fig. 5(c)) and TL4 (Fig. 5(d)), respectively.

As evident from Fig. 5, the TL projections are fully electroporated using configurations which automatically adapt number and positions of the electrodes to the TL geometry.

Each activated couple is a side of the Delaunay triangulation obtained with the electrode configuration. As required, the side length is between 5 and 30 mm. Calculation times, using a PC 3.5 GHz Intel Core i7-7800X CPU, were 56 s, 138 s, 218 s and 159 s for TL1, TL2, TL3, and TL4, respectively, including the time required for the files saving. These times are shorter than those shown in [35], [36] for E-field calculation with 6 electrodes, which are of the order of tens of minutes.

As for the longitudinal coverage, taking as examples TL2 and TL4, the  $Z_{TOT}$  of the calculated poration mask is smaller than the TL dimension along the  $z$  axis, i.e., 4.5 e 6 cm, respectively. Therefore, to fully electroporate TL2 and TL4, the treatment must be repeated after one (for TL2) or two (for TL4) deployments with 20 mm of shifts of the electrodes' tips along the  $z$  axis. Fig. 6 shows the maximum E field induced during the treatment in the  $xz$  plane. Dotted green curves are the contours of the TL sections on the  $xz$  plane, whereas dotted black curves are the contours of the TL projections on the same plane that passes through the electrodes 1, 4 and 7, in the case of TL2, and through the electrodes 1, 4, 7, and 10, for the TL4 (see Fig. 5(b) and (d), respectively). The electrodes are also depicted with the shifts associated to each deployment. Firstly, the electrodes are placed in the deepest position and the treatment is delivered, then, they are moved up of 20 mm and the treatment is repeated. For the TL4, the treatment is repeated again after another shift of

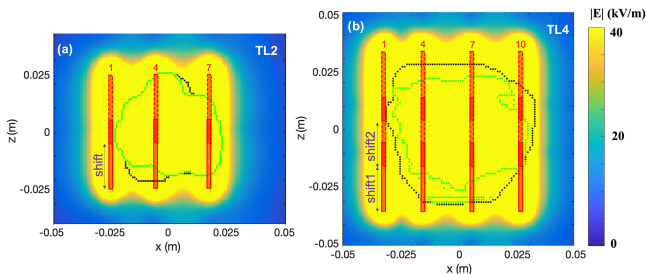


Fig. 6. Longitudinal configurations of the needles for TL2 (panel a) and TL4 (panel b), requiring one and two deployments, respectively, and induced E field on the  $xz$  plane; dotted green and black lines delimit the  $xz$  cross section of the TLs and the TL projections on the  $xz$  plane, respectively. The electrodes lying in this plane (red) are shown in their original position and after the shifts.

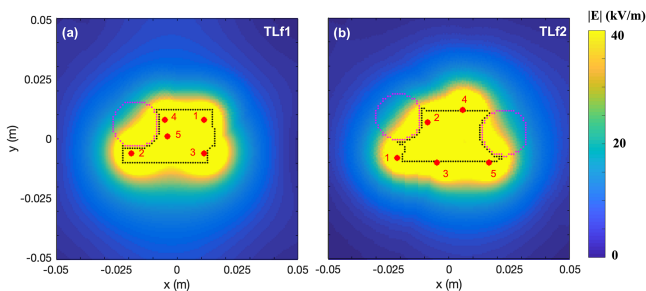


Fig. 7. Examples of electrode configurations (red dots) and induced E field in the transversal  $xy$  plane for TLf1 (panel a) and TLf2 (panel b); dotted black and magenta lines delimit the TL and the FR projections on the  $xy$  plane, respectively.

20 mm. Although this procedure prolongs the overall treatment time, it does not increase its invasiveness.

Finally, two examples of cases with FRs close to the TL are shown in Fig. 7. TLf1 (Fig. 7(a)) and TLf2 (Fig. 7(b)) exhibit one and two FRs, respectively, whose contours are marked by dotted magenta lines. In both cases, the calculated needles configurations guarantee the full coverage of the TLs transversal sections while preserving FRs from the needle passage. Calculation times were 87 s and 96 s for TLf1 and TLf2, respectively.

In all the tested cases, the electrode configurations guaranteed the full compliance with all the specifications. The calculation time ranged from some seconds to a few minutes, depending on the ROI size and shape (e.g., jagged or elongated geometry).

#### IV. DISCUSSION

Supporting tools to perform individual treatment planning are key for the effectiveness of ECT using variable electrodes configuration. In fact, EP parameters should be set to maximize the treatment effectiveness in the target volume, while preserving surrounding healthy tissue with accurate electrode placement and tailored E field inside and around the tumor [37].

Dedicated supporting tools were proposed in the literature. The first one is the preoperative planning software PULSAR (IGEA S.p.A., Carpi (MO), Italy) with the functionality to propose, before the treatment, an optimized placement of the electrodes within or around a predefined 2D area segmented by the user [37]. The strength of this tool is a workflow optimized for ease of use by the physician: DICOM image import, treatment

area definition, optimization of electrode placement, possibility to manually determine positions of the electrodes, intuitive separation of large cases into groups of no more than 6 electrodes per individual treatment, exported treatment plan file ready to be used in Cliniporator device (IGEA S.p.A., Carpi (MO), Italy).

Another tool is Visifield, a user-friendly web-based software for automatic 3D visualization of the E-field distribution in tissues, based on radiological images [https://www.visifield.com/]. Also this web-based tool is intended to facilitate the treatment planning process and to reduce the time needed for it. However, the electrodes position is an input from the user and the outputs file that contains the optimized treatment parameters could not be imported directly on the E pulse generator.

Another tool recently developed is the EView online platform for 3D E-field calculation in EP-based treatments using needle-shaped electrodes [35], [https://eview.upf.edu/]. EView provides an easy way to obtain approximate estimations of the E-field distribution for arbitrary electrode positions and orientations which represent software inputs. EView has been developed with the aim of facilitating the understanding of how the E-field distribution depends on the geometry of the electrode setup and the applied voltage.

Recently, PIRET, another integrated platform for treatment planning of irreversible EP, has been published [36], which calculates the induced E field in a 3D model obtained from patient medical images. All these latter platforms do not perform an a priori automatic estimate of the optimal electrode configuration and are only suitable for informative uses.

Implementing pretreatment planning to achieve the optimal 3D electrode configuration ensures complete EP of the ROI and optimal E-field distribution while minimizing the number of electrodes. Furthermore, the use of minimally invasive surgical approach such as percutaneous and laparoscopic approach can be used through real-time image-guided (CT, MRI or Ultrasound) electrode insertion to allow accurate electrode placement based on the treatment plan. The software illustrated in this paper overcomes the main limitations of the aforementioned supporting tools. Making use of new and original solutions, it improves the performance of PULSAR [37] in terms of realism, by operating in a 3D domain while maintaining comparable computation time. With respect to Visifield [https://www.visifield.com/], EView [35], [https://eview.upf.edu/] and PIRET [36], the main advantage is the automatic calculation of the electrodes positioning. This avoids the waste of time of testing different electrodes positions allowing the direct use, in real-time, inside the operating room.

Moreover, it is fully integrated in the pulse generator and is specifically developed to be used in clinical treatments.

#### V. CONCLUSION

In this paper, we propose an innovative code which performs an automatic 3D optimization of the electrode configuration for ECT. It takes as input the ROI and FRs, properly identified and segmented from diagnostic images (MRI, CT scan, etc.) of the patient, the electrode type and the position of possible fixed

electrodes; it calculates in real-time the best electrode configuration, with the list of activated couples, in a completely automated way and returns an accurate estimate of the E field in the whole 3D analysis domain. This will allow, in the future, the possibility of implementing a solution with the tissue conductivity dependent on the EP level.

Thanks to an innovative strategy based on the buildup of a database, where elementary E-field distributions are stored, and on an optimization technique borrowed from geometric tessellation, it reconciles accuracy and speed of computation.

Tested on a significant set of actual TLs with different size and geometry, it fulfilled all the requirements, even in complicate cases including fixed electrodes and more than one FRs. In all the tested cases, the calculation time ranged from several seconds to a few minutes.

Such software, interfaced with the hardware for the E pulse generation, automatically returns a file where all the treatment parameters are stored, offering the best technology to support medical skills. The final result is a user-friendly and versatile tool for ECT treatment planning, exhibiting significant improvements with respect to the literature.

## REFERENCES

- [1] M. Belehradek, C. Domenge, B. Lubinski, S. Orłowski, J. Jr Belehradek, and L. M. Mir, "Electrochemotherapy, a new antitumor treatment. First clinical phase I-II trial," *Cancer*, vol. 72, no. 12, pp. 3694–3700, 1993, doi: [10.1002/1097](#).
- [2] L. M. Mir et al., "L'électrochimiothérapie, un nouveau traitement antitumoral: Premier essai clinique [Electrochemotherapy, a new antitumor treatment: First clinical trial]," *C. R. Acad. Sci. III*, vol. 313, no. 13, pp. 613–618, 1991.
- [3] S. Theurich et al., "Local tumor treatment in combination with systemic Ipilimumab immunotherapy prolongs overall survival in patients with advanced malignant melanoma," *Cancer Immunol. Res.*, vol. 4, pp. 744–754, 2016, doi: [10.1158/2326-6066.CCR-15-0156](#).
- [4] B. Karaca, G. Yayla, M. Erdem, and T. Gürlür, "Electrochemotherapy with anti-PD-1 treatment induced durable complete response in heavily pretreated metastatic melanoma patient," *Anticancer Drugs*, vol. 28, no. 2, pp. 190–196, 2018, doi: [10.1097/CAD.0000000000000580](#).
- [5] R. Cadossi, M. Ronchetti, and M. Cadossi, "Locally enhanced chemotherapy by electroporation: Clinical experiences and perspective of use of electrochemotherapy," *Future Oncol.*, vol. 10, no. 5, pp. 877–890, 2014.
- [6] C. A. Goggins and A. Khachemoune, "The use of electrochemotherapy in combination with immunotherapy in the treatment of metastatic melanoma: A focused review," *Int. J. Dermatol.*, vol. 58, no. 8, pp. 865–870, 2019.
- [7] L. M. Mir et al., "Standard operating procedures of the electrochemotherapy: Instructions for the use of bleomycin or cisplatin administered either systemically or locally and electric pulses delivered by the Cliniporator™ by means of invasive or non-invasive electrodes," *Eur. J. Cancer Suppl.*, vol. 4, pp. 14–25, 2006, doi: [10.1016/j.ejcsup.2006.08.003](#).
- [8] J. Gehl et al., "Updated standard operating procedures for electrochemotherapy of cutaneous tumours and skin metastases," *Acta Oncol.*, vol. 57, no. 7, pp. 874–882, 2018, doi: [10.1080/0284186X.2018.1454602](#).
- [9] B. Mali, T. Jarm, M. Snoj, G. Sersa, and D. Miklavcic, "Antitumor effectiveness of electrochemotherapy: A systematic review and meta-analysis," *Eur. J. Surg. Oncol.*, vol. 39, pp. 4–16, 2013, doi: [10.1016/j.ejso.2012.08.016](#).
- [10] F. Izzo et al., "Clinical phase I/II study: Local disease control and survival in locally advanced pancreatic cancer treated with electrochemotherapy," *J. Clin. Med.*, vol. 10, no. 6, 2021, Art. no. 1305, doi: [10.3390/jcm10061305](#).
- [11] M. Marty et al., "Electrochemotherapy—An easy, highly effective and safe treatment of cutaneous and subcutaneous metastases: Results of ESOPE (European Standard Operating Procedures of Electrochemotherapy) study," *Eur. J. Cancer Suppl.*, vol. 4, no. Suppl. S4, pp. 3–13, 2006, doi: [10.1016/j.ejcsup.2006.08.002](#).
- [12] L. G. Campana et al., "Bleomycin-based electrochemotherapy: Clinical outcome from a single institution's experience with 52 patients," *Ann. Surg. Oncol.*, vol. 16, pp. 191–199, 2009, doi: [10.1245/s10434-008-0204-8](#).
- [13] L. G. Campana et al., "Electrochemotherapy for disseminated superficial metastases from malignant melanoma," *J. Brit. Surg.*, vol. 99, pp. 821–830, 2012, doi: [10.1002/bjs.8749](#).
- [14] D. E. Spratt et al., "Efficacy of skin-directed therapy for cutaneous metastases from advanced cancer: A meta-analysis," *J. Clin. Oncol.*, vol. 32, pp. 3144–3155, 2014, doi: [10.1200/JCO.2014.55.4634](#).
- [15] M. J. Aguado-Romeo, S. Benot-López, and A. Romero-Tabares, "Electrochemotherapy for the treatment of unresectable locoregionally advanced cutaneous melanoma: A systematic review," *Actas Dermosifiliogr.*, vol. 108, pp. 91–97, 2017, doi: [10.1016/j.ad.2016.08.008](#).
- [16] C. C. Plaschke, A. Gothelf, J. Gehl, and I. Wessel, "Electrochemotherapy of mucosal head and neck tumours: A systematic review," *Acta Oncol.*, vol. 55, pp. 1266–1272, 2016, doi: [10.1080/0284186X.2016.1207803](#).
- [17] R. Rotunno et al., "Electrochemotherapy in non-melanoma head and neck skin cancers: A three-center experience and review of the literature," *G. Ital. Dermatol. Venereol.*, vol. 151, pp. 610–618, 2016.
- [18] L. Tarantino et al., "Percutaneous electrochemotherapy in the treatment of portal vein tumor thrombosis at hepatic hilum in patients with hepatocellular carcinoma in cirrhosis: A feasibility study," *World J. Gastroenterol.*, vol. 23, no. 5, pp. 906–991, 2017, doi: [10.3748/wjg.v23.i5.906](#).
- [19] B. Mali et al., "Electrochemotherapy of colorectal liver metastases—an observational study of its effects on the electrocardiogram," *Biomed. Eng. Online*, vol. 14, no. Suppl. S3, 2015, Art. no. S5, doi: [10.1186/1475-925X-14-S3-S5](#).
- [20] I. Edhemovic et al., "Intraoperative electrochemotherapy of colorectal liver metastases," *J. Surg. Oncol.*, vol. 110, no. 3, pp. 320–327, 2014, doi: [10.1002/jso.23625](#).
- [21] R. Girelli et al., "Feasibility and safety of electrochemotherapy (ECT) in the pancreas: A pre-clinical investigation," *Radiol. Oncol.*, vol. 49, no. 2, pp. 147–154, 2015, doi: [10.1515/raon-2015-0013](#).
- [22] M. J. Jaroszeski, P. Illingworth, C. Pottinger, M. Hyacinthe, and R. Heller, "Electrically mediated drug delivery for treating subcutaneous and orthotopic pancreatic adenocarcinoma in a hamster model," *Anticancer Res.*, vol. 19, pp. 989–994, 1999.
- [23] V. Granata et al., "Electrochemotherapy in locally advanced pancreatic cancer: Preliminary results," *Int. J. Surg.*, vol. 18, pp. 230–236, 2015, doi: [10.1016/j.ijso.2015.04.055](#).
- [24] V. Granata et al., "Early radiological assessment of locally advanced pancreatic cancer treated with electrochemotherapy," *World J. Gastroenterol.*, vol. 23, pp. 4767–4778, 2017, doi: [10.3748/wjg.v23.i26.4767](#).
- [25] G. Ranieri et al., "Local treatment with deep percutaneous electrochemotherapy of different tumor lesions: Pain relief and objective response results from an observational study," *Eur. Rev. Med. Pharmacol. Sci.*, vol. 24, no. 14, pp. 7764–7775, 2020, doi: [10.26355/eurrev\\_202007\\_22279](#).
- [26] D. Miklavcic Ed. *Handbook of Electroporation*. Cham, Switzerland: Springer, 2017.
- [27] D. Miklavcic and R. V. Davalos, "Electrochemotherapy (ECT) and irreversible electroporation (IRE) - advanced techniques for treating deep-seated tumors based on electroporation," *Biomed. Eng. Online*, vol. 14, no. Suppl 3, 2015, Art. no. 11.
- [28] D. Pavliha et al., "Electroporation-based treatment planning for deep-seated tumors based on automatic liver segmentation of MRI images," *PLoS One*, vol. 8, no. 8, 2013, Art. no. e69068.
- [29] V. Granata et al., "Electroporation-based treatments in minimally invasive percutaneous, laparoscopy and endoscopy procedures for treatment of deep-seated tumors," *Eur. Rev. Med. Pharmacol. Sci.*, vol. 25, no. 9, pp. 3536–3545, 2021, doi: [10.26355/eurrev\\_202105\\_25836](#).
- [30] A. Denzi et al., "Modeling the positioning of single needle electrodes for the treatment of breast cancer in a clinical case," *Biomed. Eng. Online*, vol. 14, 2015, Art. no. S1.
- [31] B. Kos, A. Zupanic, T. Kotnik, M. Snoj, G. Sersa, and D. Miklavcic, "Robustness of treatment planning for electrochemotherapy of deep-seated tumors," *J. Membr. Biol.*, vol. 236, no. 1, pp. 147–153, 2010.
- [32] D. Pavliha, B. Kos, A. Zupanic, M. Marčan, G. Serša, and D. Miklavcic, "Patient-specific treatment planning of electrochemotherapy: Procedure design and possible pitfalls," *Bioelectrochemistry*, vol. 87, pp. 265–273, 2012.
- [33] M. Marcan et al., "Web-based tool for visualization of electric field distribution in deep-seated body structures and planning of electroporation-based treatments," *Biomed. Eng. Online*, vol. 14, no. Suppl 3, 2015, Art. no. S4.

- [34] M. Marcan et al., "Segmentation of hepatic vessels from MRI images for planning of electroporation-based treatments in the liver," *Radiol. Oncol.*, vol. 48, no. 3, pp. 267–281, 2014.
- [35] E. Perera-Bel et al., "EView: An electric field visualization web platform for electroporation-based therapies," *Comput. Methods Programs Biomed.*, vol. 197, 2020, Art. no. 105682.
- [36] E. Perera-Bel et al., "PIRET-A platform for treatment planning in electroporation-based therapies," *IEEE Trans. Biomed. Eng.*, vol. 70, no. 6, pp. 1902–1910, 2023.
- [37] U. Probst et al., "Electrochemotherapy as a new modality in interventional oncology: A review," *Technol. Cancer Res. Treat.*, vol. 17, 2018, Art. no. 1533033818785329.
- [38] F. Liu, H. Zhao, and S. Crozier, "On the induced electric field gradients in the human body for magnetic stimulation by gradient coils in MRI," *IEEE Trans. Biomed. Eng.*, vol. 50, no. 7, pp. 804–815, 2003.
- [39] A. Paffi et al., "A computational model for real-time calculation of electric field due to transcranial magnetic stimulation in clinics," *Int. J. Antennas Propag.*, vol. 2015, 2015, Art. no. 976854.
- [40] M. S. Shephard, H. L. de Cougny, R. M. O'Bara, and M. W. Beall, "Automatic grid generation using spatially based trees," in *Handbook of Grid Generation*, J. F. Thompson, B. K. Soni, and N. P. Weatherill, Eds. Boca Raton, FL: CRC Press, 1999, ch. 15, pp. 1–19.
- [41] J. N. Reddy, *An Introduction to the Finite Element Method*, 3rd ed. New York, NY, USA: McGraw-Hill, 2006.
- [42] P. O. Persson and G. Strang, "A simple mesh generator in MATLAB," *SIAM Rev.*, vol. 46, no. 2, pp. 329–345, 2004.
- [43] B. Delaunay, "Sur la sphère vide. Bulletin de l'Académie des Sciences de l'URSS," *Classe des Sci. Mathématiques et Naturelles*, vol. 6, pp. 793–800, 1934.